




Synthesis and study of the structural and dielectric properties of $\text{La}_{0.67}\text{Ca}_{0.2}\text{Ba}_{0.13}\text{Fe}_{1-x}\text{Mn}_x\text{O}_3$ ferrites ($x = 0, 0.03$ and 0.06)

A. Dhahri^{1,2}, A. Zaouali³, A. Benali^{1,2,4}, N. Abdelmoula², J. Massoudi², K. Nouri^{5,6}, L. Bessais⁵, M. P. F. Graça⁴, M. A. Valente⁴, and B. F. O. Costa^{1,*} 

¹CFisUC, Physics Department, University of Coimbra, Rua Larga, 3004-516 Coimbra, Portugal

²Laboratoire de Physique Appliquée, Faculté des Sciences, Université de Sfax, B.P. 1171, 3000 Sfax, Tunisia

³Laboratoire des Matériaux Multifonctionnels et Applications, Faculté des Sciences, Université de Sfax, 3000 Sfax, Tunisia

⁴IN and Physics Department, University of Aveiro, 3810-193 Aveiro, Portugal

⁵CMTR, ICMPE, UMR 7182 CNRS-UPEC, 2 rue Henri Dunant, 94320 Thiais, France

⁶Altran, 2 rue Paul Dautier, 78140 Vélizy-Villacoublay, France

Received: 3 November 2020

Accepted: 7 February 2021

Published online:

26 February 2021

© The Author(s), under exclusive licence to Springer Science+Business Media, LLC part of Springer Nature 2021

ABSTRACT

The $\text{La}_{0.67}\text{Ca}_{0.2}\text{Ba}_{0.13}\text{Fe}_{1-x}\text{Mn}_x\text{O}_3$ perovskite compounds with different manganese concentrations ($x = 0.0, 0.03, 0.06$) were synthesized by the autocombustion method and annealed at 700 °C. The X-ray diffraction (XRD) data indicated that all obtained compounds crystallize in the cubic structure with the $\text{Pm}\bar{3}\text{m}$ space group. The increase in the substitution rate has been found to lead to the decrease in the crystallite size value characterized by X-ray diffraction. The dielectric properties of these samples, using a complex impedance spectroscopy technique, were also performed as a function of frequency and temperature. A suitable equivalent electrical circuit was used to assess the contributions of electrode, grains, and grain boundaries in the complex impedance results. Activation energies were determined from different methods. Nyquist plots were consistent with three circuits in series, each one with a capacitance in parallel with a resistance. The conduction mechanism follows the NSPT model for the three samples at $T < 280$ K, in which the rise in substitution rate increases the binding energy of carriers. Above 280 K, the appropriate model is the Correlated Barrier Hopping (CBH) for $x = 0$, while the overlapping large polaron tunneling (OLPT) process has been confirmed for both samples $x = 0.03$ and $x = 0.06$. Our compounds have high electrical properties, and good thermal and chemical stability. They are susceptible to many technological applications, such as gas sensors, capacitors, filters, resonators, new read heads, and solid oxide fuel cells.

Address correspondence to E-mail: benilde@uc.pt

1 Introduction

In the past few decades, orthoferrites have received particular attention thanks to their wide range of applications [1]. Iron oxide LaFeO₃ is one of the most important orthoferrites with high stability over a wide temperature range [2]. Ferrites, belonging to mixed metal oxide systems, are generally represented by ABO₃, where A and B are generally divalent and trivalent atoms [3]. The depletion of conventional energy resources has multiplied the demand for smarter production and storage of energy systems. The encouraging energy storage entities are supercapacitors and lithium batteries [4, 5], which are very expensive. Ferrites are very promising because of their low cost and electrochemical properties [6]. They have already shown to be adequate in fuel cells, lithium batteries, and supercapacitors [7].

The LaFeO₃ compounds substituted in A-site and B-site with the general formula of La_{1-x}A_xFeO₃ and LaFe_{1-x}B_xO₃ have been studied thanks to their extensive usage in applications. Due to their important physical properties, La_{1-x}A_xFe_{1-y}M_yO_{3-d} compounds (A = Ca, Sr, Ba..., M = Mn, Ti, Cr, Co...) are used in many applications, such as toxic gas detection materials [8–10], oxygen dense membrane [11–13], oxygen sensor [14], batteries [15], solid oxide fuel cells (SOFCs) [16–22], and catalytic materials [23, 24]. Different elaboration methods have been used to synthesize lanthanum ferrites, such as the solid-state reaction, co-precipitation, Sol–Gel, and hydrothermal [25].

Cao et al. [26] and Phokha et al. [27] found that the introduction of a transition metal into the A- and B-sites of LaFeO₃ improves their physical properties. Sun et al. [28] studied the structural and electrical properties of the nanocrystalline La_{1-x}Ba_xFeO₃ compounds and found that the insertion of the Ba ion into the A-site can restrain the growth of grain size and enhance the response to ethanol gas. The best response to ethanol gas was obtained for a rate equal to 0.25 mol of Ba. Other detailed dielectric studies [29] have shown that the La_{1-x}Ba_xFeO₃ system exhibits high dielectric permittivity.

Previous studies [30] have confirmed that the appropriate amount of substitution in site A is almost 20%. In the case of double substitutions in A-site, an amount of 10% for each inserted ion improves the physicochemical properties of substituted ferrites [31–33].

Benali et al. [34] studied the dielectric properties of LaCaFeO₃ and they showed that the electrical conduction mechanism is governed by the small non-overlapping polaron tunnel (NSPT) model.

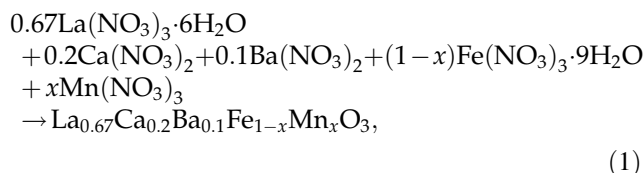
Ferrites, having a transition metal at the B-site, have a greater tendency to occupy more than one oxidation state which affects their chemical and physical properties. The charge hop between cations at octahedral sites is the source of electrical conduction in these ferrite systems. The presence of mixed valence cations at octahedral sites improves electrical conductivity [35]. In this paper, we investigated the AC electrical conduction mechanism of La_{0.67}Ca_{0.2}Ba_{0.13}Fe_{1-x}Mn_xO₃. To our knowledge, no such study of this material has been reported yet. Complex impedance spectroscopy is a powerful tool to analyze the grains (intrinsic) and grain boundaries (extrinsic) contributions to the electric properties of the material.

In the present work, the La_{0.67}Ca_{0.2}Ba_{0.13}Fe_{1-x}Mn_xO₃ compounds were synthesized via the auto-combustion technique. The effect of the fuel–oxidant ratio on the combustion process and the quality of obtained products was interesting. In addition, the effects of manganese doping on the structural, microstructure, dielectric properties, and conduction mechanism of the prepared La_{0.67}Ca_{0.2}Ba_{0.13}Fe_{1-x}Mn_xO₃ compounds were studied.

2 Experimental details

2.1 Synthesis

The reagents used in the reaction were of analytical grade. The oxidants are Lanthanum nitrate La(NO₃)₃·6H₂O, Calcium nitrate Ca(NO₃)₂, Barium nitrate Ba(NO₃)₂, Manganese nitrate Mn(NO₃)₃, and Ferric nitrate Fe(NO₃)₃·9H₂O obtained from Sigma-Aldrich, Germany. The La_{0.67}Ca_{0.2}Ba_{0.1}Fe_{1-x}Mn_xO₃ (x = 0.0, 0.03, and 0.06) perovskite compounds were synthesized by the autocombustion method according to the following reaction equation:



The metal nitrates were first dissolved in distilled water at a stoichiometric ratio and stirred thoroughly

at room temperature for 1 h. Then, glycine (G , $C_2H_5NO_2$) obtained from SD Fine Chem. Ltd., Mumbai, was added to the mixture as a fuel agent. The amount of the used fuel was calculated on the basis of the Glycine to metal ions ratio: $G/M = 1.2$ (rich fuel composition), which is greater than the stoichiometric quantity required to complete the combustion process without heat exchange. The temperature of the mixture was raised to $80\text{ }^\circ\text{C}$ and a viscous gel was formed and annealed at $180\text{ }^\circ\text{C}$ to form a dry gel. After that, the self-combustion took place at $300\text{ }^\circ\text{C}$, which originated a black powder. The resulting pellets were sintered at $700\text{ }^\circ\text{C}$.

2.2 Characterization methods

The X-ray diffractograms of the autocombustion powders were recorded using an X-ray diffractometer (D8 ADVANCE, Bruker), equipped with a $CuK\alpha$ radiation source ($\lambda = 1.5406\text{ \AA}$) in θ - 2θ Bragg–Brentano geometry. The acquisition was in the range of 5 – 90° , with a step of 0.02° and an acquisition time for each step of 1 s XRD. Data were subsequently refined by the Rietveld method [36], using the FULLPROF software [37] to obtain network parameters. Scanning electron micrographs (SEM) were taken with TESCAN VEGA3 SBH microscope equipped with an EDS detector Bruker XFlash 410M. In this way, energy-dispersive X-ray analysis (EDXA) was also done.

Thermal analysis was done by Differential Scanning Calorimetry (DSC) performed using a PerkinElmer STA6000 system, with a step of $10\text{ }^\circ\text{C}/\text{min}$ and nitrogen flux. With this system, both sample and reference are measured simultaneously, which is an advantage. The dielectric measurements were performed in air using an impedance spectrometer. For these measurements, a Network Analyzer Agilent 4294, operating between 100 Hz and 1 MHz in the Cp–Rp configuration (capacitance in parallel with resistance), was used [38]. During the measurement, the pellet was mechanically compressed between two parallel platinum plates functioning as electrodes.

3 Results and discussion

3.1 Structural study

The room-temperature X-ray pattern for $La_{0.67}Ca_{0.2}Ba_{0.13}Fe_{1-x}Mn_xO_3$ compounds ($x = 0.00, 0.03$ and

0.06) displayed in Fig. 1a revealed that all samples show the same perovskite structure. All peaks are identical and superimposable which can be assigned to the diffraction lines of the cubic $LaFeO_3$ phase (JCPDS file COD 96-154-2145). No additional peak was observed by the substitution of the Fe^{3+} ions by the Mn^{3+} ions. All peaks are well indexed to 2θ values of $22.7^\circ, 32.4^\circ, 39.9^\circ, 46.5^\circ, 57.68^\circ, 67.8^\circ, 77.1^\circ, 81.6^\circ, 86.1^\circ$, and 95.1° indicating the 100, 110, 111, 200, 210, 211, 220, 310, 222, and 321 crystal planes, respectively. All obtained compounds crystallize in the cubic structure with the $Pm\bar{3}m$ space group. From the XRD patterns, it can be seen that the intensity of the most intense peak [110] increased with the dopant content, which could be due to a distortion of the lattice and to a better crystallinity. Also, the patterns exhibited a slight shift of the most intense peak towards smaller 2θ values (Fig. 1b) when the Mn content increased; this indicates that Mn has a larger ionic radius than Fe. The shift of diffraction peaks toward lower angle revealed that the cell parameters of samples increase with the increase of Mn content. A typical Rietveld refinement analysis of $x = 0.06$ sample, using FullProf software [37], is shown in Fig. 1c. The results of the refinement of the structural parameters of our samples are reported in Table 1. A low increase in cell volume is observed when doping. The unit cell volume remains constant when $x = 0.03$ and 0.06 . If the manganese and the iron were in a high-spin state, their ionic radii were equal to 0.645 \AA , and then the volume and the lattice parameter remain invariant. The low volume increase shows that the Mn and Fe are in a low-spin state, whose ionic radii are 0.58 \AA and 0.55 \AA , respectively [39].

The crystallite size of all samples was determined from full width half maximum (FWHM) of the most intense peak of the X-ray spectrum, corresponding to the (110) plane using the Debye–Scherrer formula: [40]:

$$D_{SC} = \frac{K \times \lambda}{\beta \times \cos \theta}, \quad (2)$$

where D_{SC} is the crystal size; K is a dimensionless shape factor with a value 0.9; λ is the wavelength of $CuK\alpha_1$ (1.5406 \AA); θ is the Bragg angle (in degrees); and β is the line broadening at half the maximum intensity (FWHM), after subtracting the instrumental line broadening, in radians. The sizes of the

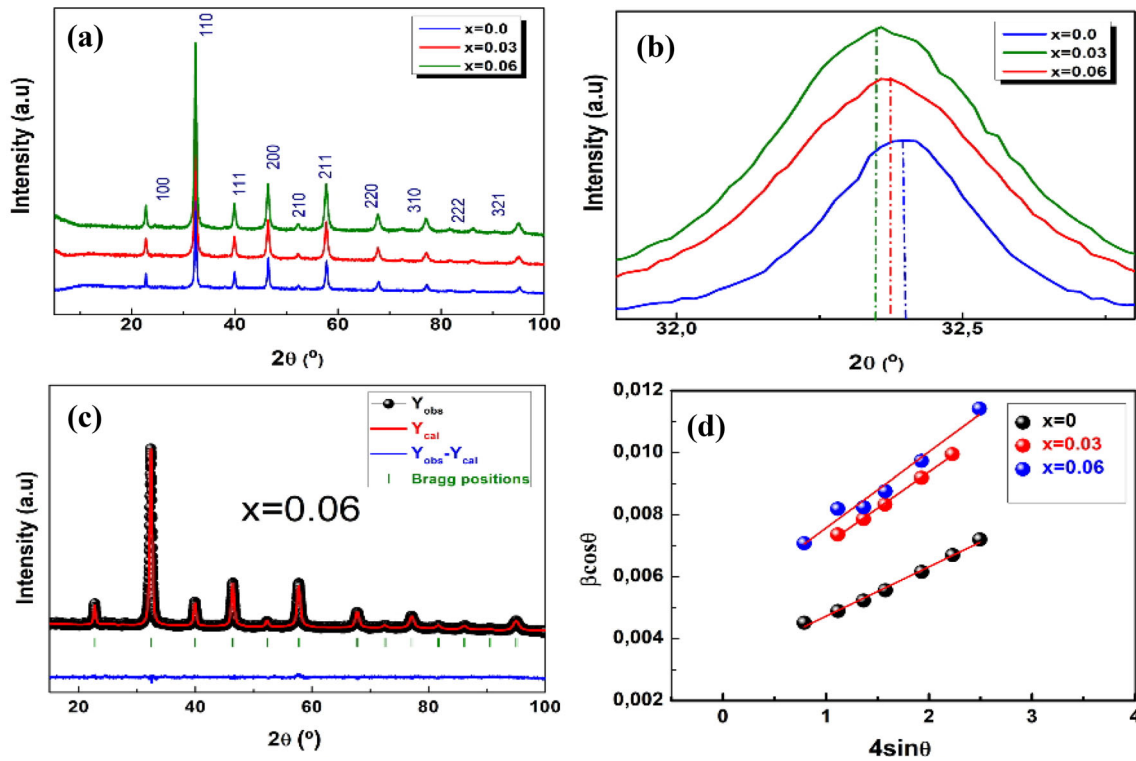


Fig. 1 **a** XRD patterns for the three samples, **b** most intense peak of the patterns, **c** Rietveld refinement analysis of $x = 0.06$ sample pattern and **d** W–H plots of $\text{La}_{0.67}\text{Ca}_{0.2}\text{Ba}_{0.13}\text{Fe}_{1-x}\text{Mn}_x\text{O}_3$ compounds ($x = 0.00, 0.03$ and 0.06)

Table 1 Structural parameters such as, lattice constant (a), X-ray density ($\rho_{\text{X-ray}}$), bulk density (ρ_{exp}), porosity (P), crystallite size determined by Scherrer formula (D_{SC}) and by Williamson–Hall method ($D_{\text{W-H}}$), specific surface area (S), and number of defects (δ)

Sample	a (Å)	Volume (Å ³)	$\rho_{\text{X-ray}}$ (g/cm ³)	ρ_{exp} (g/cm ³)	P (%)	D_{SC} (nm)	$D_{\text{W-H}}$ (nm)	S (m ² /g)	$\delta \cdot 10^{-4}$ (nm ⁻²)
$x = 0$	3.906 ₃	59.606 ₉	6.206	3.252	47.599	28	44	21.973	5.165
$x = 0.03$	3.911 ₅	59.846 ₉	6.182	3.006	51.375	19	29	33.468	11.891
$x = 0.06$	3.911 ₆	59.848 ₉	6.181	3.067	50.380	17	27	35.953	13.717

crystallites are approximately 44 nm, 29 nm, and 27 nm for $x = 0, 0.03$, and 0.06 respectively.

The Williamson–Hall (W–H) plots of the 3 compounds are shown in Fig. 1d. These plots provide a linear relationship between $\beta\cos\theta$ and $4\sin\theta$ and the slope provides the induced strain (ϵ). The size of the crystallites ($D_{\text{W-H}}$) is deduced from the intercept of the line with the y -axis. We notice that the straight line intercepts all the points, asserting a uniform particle size distribution of the crystallites and a very low deformation. The average size of the crystallites determined by both Williamson–Hall method and Scherrer formula is reported in Table 1 for the three compounds. It is clear that the $D_{\text{W-H}}$ value calculated

using the Williamson–Hall method is higher than the one obtained using the Scherrer equation D_{SC} . The Williamson–Hall equation takes into consideration all diffraction peaks and assumes the broadening of it, that is related to the crystalline size as well as the lattice strain, which is not considered in the Scherrer equation [41].

The different parameters, like bulk density ρ_{exp} , X-ray density $\rho_{\text{X-ray}}$, and porosity P values, were calculated and are listed in Table 1. It is observed that by increasing dopant concentration the porosity (P) increases and the X-ray density ($\rho_{\text{X-ray}}$) is reduced. This decline in X-ray density with the substitution

can be attributed to smaller weight of dopant Mn (54.938 amu) as compared to Fe (55.847 amu) [42, 43].

X-ray density ($\rho_{X\text{-ray}}$) was calculated taking into consideration that a basic unit cell of the cubic perovskite structure contained eight ions according to the following formula [44]:

$$\rho_{X\text{-ray}} = \frac{4M}{VN_A}, \quad (3)$$

where 4 is the number of molecules in a unit cell of perovskite lattice, M is the molecular weight of each compound, V is the as-calculated lattice parameter converted in cm units, and N_A is Avogadro's number.

The bulk density ρ_{exp} estimated using the following relation [45]:

$$\rho_{\text{exp}} = \frac{m}{\pi \cdot r^2 \cdot h}, \quad (4)$$

where h , r , and m are the thickness, the radius, and the mass of pellet, respectively.

The notion of porosity has been attributed by the difference between X-ray density and the experimental density according to the following formula [46]:

$$P(\%) = \frac{\rho_{X\text{-ray}} - \rho_{\text{exp}}}{\rho_{X\text{-ray}}} \times 100. \quad (5)$$

Assuming that all the particles are spherical, the specific surface area was calculated using the following relation [47]:

$$S = \frac{6000}{D_{W-H} \cdot \rho_{\text{exp}}}, \quad (6)$$

where the constant 6000 is a form factor for spherical particles, D_{W-H} is the diameter of the particle in meter (m) calculated from Williamson–Hall model, and ρ_{exp} is the density in g/m^3 .

The number of defects in the sample was represented by the dislocation density (δ), which is defined as the length of the dislocation lines per unit volume of the crystal [48]:

$$\delta = \frac{1}{D_{W-H}^2}, \quad (7)$$

where D_{W-H} is the particle's diameter in nm.

The specific surface area and the porosity of the cell units show that the distribution is almost homogeneous, and the grains are agglomerated over the entire surface of the sample. The large surface area of perovskite nanoparticles may be required for the detection and application of gas sensors [49].

To validate the existence of the cubic structure of our samples, the Goldschmidt tolerance factor is calculated [50], by the following formula:

$$t_G = \frac{\langle r_A \rangle + r_O}{\sqrt{2}(\langle r_B \rangle + r_O)}, \quad (8)$$

where $\langle r_A \rangle$ is the average ionic radius of A-site, $\langle r_B \rangle$ is the average ionic radius of B-site, and r_O is the ionic radius of oxygen [39]

The calculated value of t_G was found to be 1.01 for the 3 samples, which confirms their cubic structures.

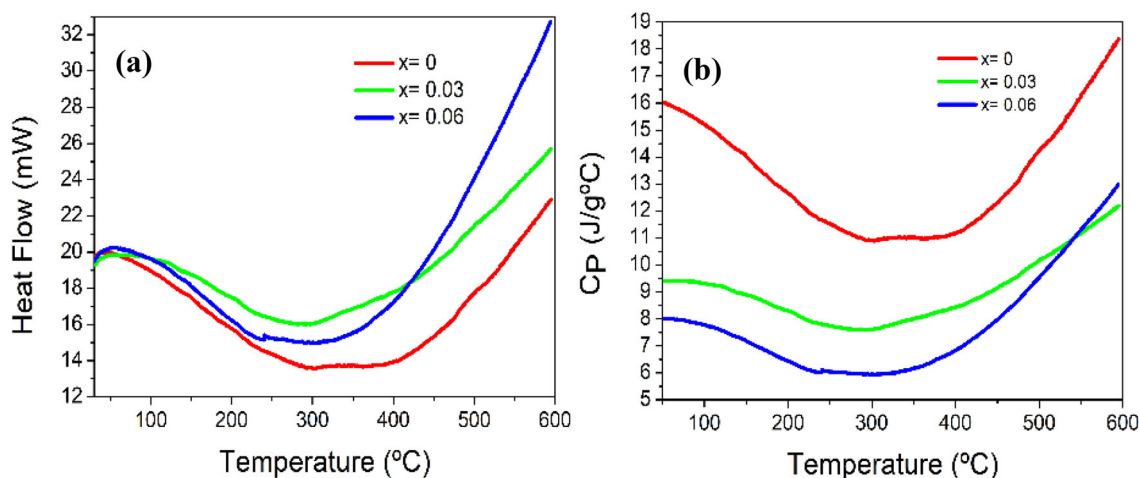


Fig. 2 **a** Heat flow Φ in function of temperature and **b** specific heat capacity (C_p) vs. temperature, of $\text{La}_{0.67}\text{Ca}_{0.2}\text{Ba}_{0.13}\text{Fe}_{1-x}\text{Mn}_x\text{O}_3$ compounds ($x = 0.00, 0.03, \text{ and } 0.06$)

3.2 Thermal analysis

Differential Scanning Calorimetry (DSC) was done to evaluate the thermal properties of the samples. Figure 2a shows the heat flow in function of temperature for the three samples. In Fig. 2b the specific heat capacity is plotted against temperature. Specific heat capacity (C_p) was determined by the equation:

$$C_p = \Phi / (m\beta), \tag{9}$$

where Φ is the heat flow, m is the mass of the sample, and β is the heating rate (10 °C/min).

In the case of LaFeO₃ perovskites, the minimum of the heat flow/heat capacity is considered the Neel temperature (T_N) [51]. T_N is 400 °C for LaFeO₃

[52, 53] and after that temperature the heat flow/ C_p increases sharply, because some of the energy is used in helping the random motions of the atoms during the transition. From Fig. 2a one can deduce T_N of about 380 °C, 300 °C, and 330 °C for $x = 0, 0.03,$ and 0.06 samples, respectively. Thus, the Mn doping decreases the T_N , but the lower value is obtained for $x = 0.03$.

In what concerns C_p , the value at RT for LaFeO₃ is 6.6 J/(g °C) [54]. In our case, we obtained 16.03, 9.47, and 7.92 J/(g °C) for $x = 0, x = 0.03,$ and $x = 0.06$ samples, respectively. Our samples have higher C_p than the pristine LaFeO₃, may be due to the existence of distortions in our samples when doping with other

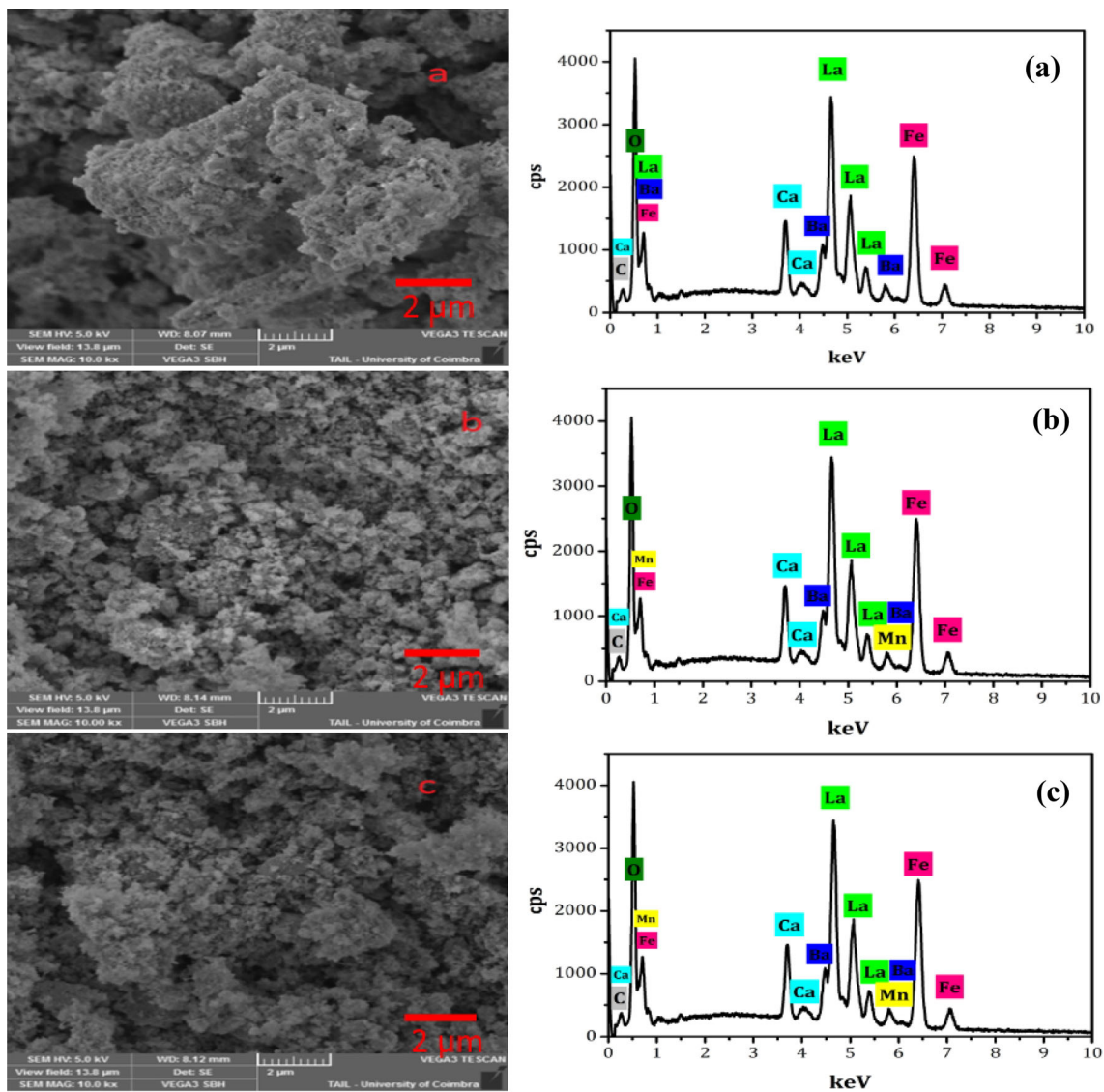


Fig. 3 SEM images and EDS analysis of La_{0.67}Ca_{0.2}Ba_{0.13}Fe_{1-x}Mn_xO₃ compounds; **a** $x = 0.00$, **b** $x = 0.03$, and **c** $x = 0.06$

elements. The Mn doping approaches C_p values to the pure LaFeO_3 value.

Comparing the doped samples 0.03 and 0.06, the increase of heat/specific heat above T_N is not so sharp in the case of the 0.03 sample. This can be due to a slight increase in porosity (see Table 1) in this sample, which increases the disorder in the sample. We can also see in Fig. 3 that the undoped sample is more compact.

3.3 Morphological study

Scanning electron microscopy (SEM) analysis was performed on the three compounds in order to study the surface morphology of these materials. The SEM images of the compounds $\text{La}_{0.67}\text{Ca}_{0.2}\text{Ba}_{0.13}\text{Fe}_{1-x}\text{Mn}_x\text{O}_3$ ($x = 0.00, 0.03$ and 0.06), in Fig. 3a, show a microstructure with an almost homogeneous

Table 2 Theoretical and experimental nominal atomic percentages obtained by EDS of the elements La, Ca, Pb, Fe, and Mn of the compounds $\text{La}_{0.67}\text{Ca}_{0.2}\text{Ba}_{0.13}\text{Fe}_{1-x}\text{Mn}_x\text{O}_3$ ($x = 0.00, 0.03$, and 0.06)

χ	La(%)		Ca(%)		Ba(%)		Fe(%)		Mn(%)	
	Theoretical	EDS	Theoretical	EDS	Theoretical	EDS	Theoretical	EDS	Theoretical	EDS
0.00	13.40	12.29	4	3.89	2.60	1.54	20.00	19.72	0.00	0.00
0.03	13.40	10.51	4	3.72	2.60	2.59	19.40	17.01	0.60	0.85
0.06	13.40	10.58	4	3.42	2.60	2.17	18.80	16.18	1.20	1.24

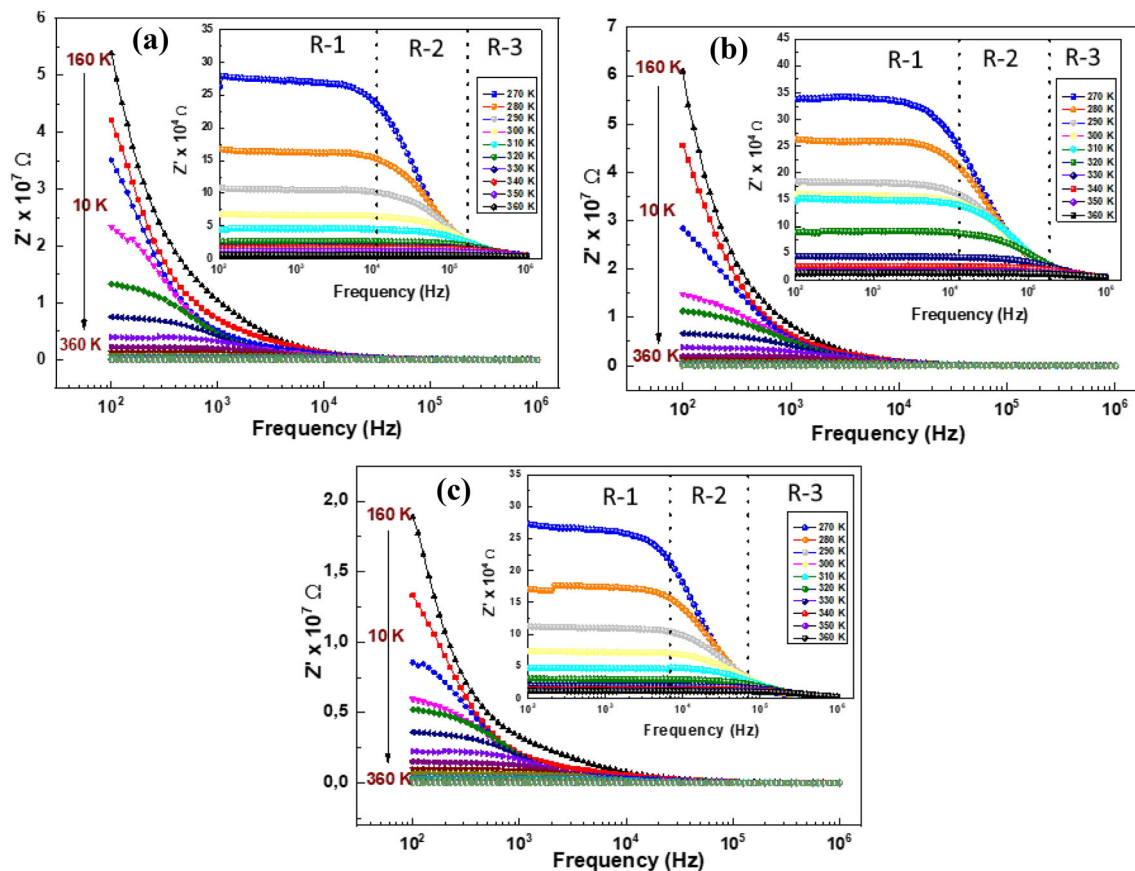


Fig. 4 The frequency dependence of the real (Z') part of the complex electrical impedance at different temperatures of $\text{La}_{0.67}\text{Ca}_{0.2}\text{Ba}_{0.13}\text{Fe}_{1-x}\text{Mn}_x\text{O}_3$ compounds: **a** $x = 0.00$, **b** $x = 0.03$, and **c** $x = 0.06$. The insets show the three distinct regions

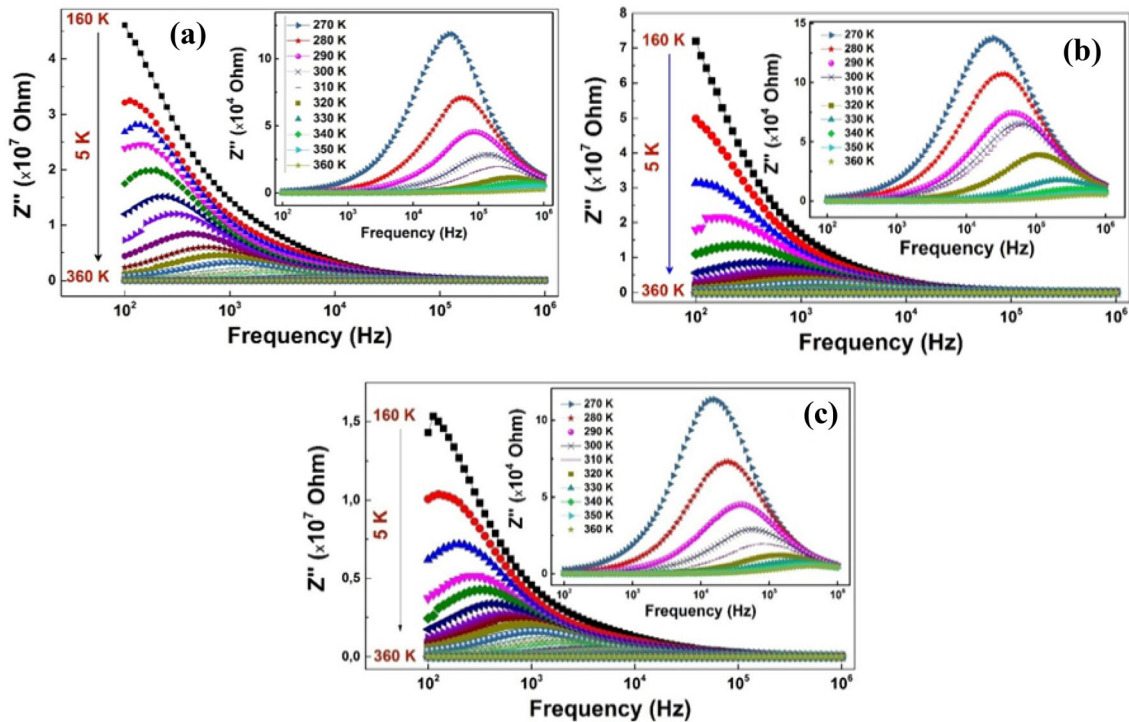


Fig. 5 The frequency dependence of the imaginary part (Z'') at several temperatures of $\text{La}_{0.67}\text{Ca}_{0.2}\text{Ba}_{0.13}\text{Fe}_{1-x}\text{Mn}_x\text{O}_3$ compounds: **a** $x = 0.00$, **b** $x = 0.03$, and **c** $x = 0.06$. Insets: displacement of peaks towards high frequencies with the increasing temperature

granular distribution. The grains are agglomerated over the entire surface of the sample.

As the doping rate increases, the porosity of the grains increases, as shown in Table 1, the morphology changes with doping. One can observe that the undoped sample is more compact in what concerns agglomeration.

The elemental analysis EDS (Energy Dispersion Spectroscopy) allows a qualitative and quantitative analysis of the elements present in the synthesized compounds. The spectra obtained (Fig. 3-EDS) reveal the presence of all the elements (La, Ca, Ba, Fe, Mn, and O) initially introduced during the preparation and that no element is volatile at 700 °C.

Nominal atomic percentages obtained by EDS associated with each element are given in Table 2. It should be noted that the compositions of the experimental samples are similar to the theoretical compositions (Table 2). Likewise, we can observe that the percentage of manganese (Mn) increases monotonically with the increase in the rate of substitution in accordance with what has been desired.

3.4 Impedance studies

Impedance spectroscopy is well known as a powerful technique for studying the relaxation processes as well as the conduction mechanism of materials. This technique is widely used to quantify the contributions that constitute these materials as well as their effects on the electrical and dielectric properties. The impedance plots of the ferrites can have one or more semicircles. Usually, in ferrites, grain boundaries are highly resistive due to the presence of a higher density of structural and chemical defects compared to grain interiors. Therefore, at high frequency, the appearance of a smaller diameter semicircle is attributed to grain interiors and larger diameter semicircle is attributed to grain boundaries [55, 56].

The variation of the real part of the impedance (Z'), as a function of frequency with temperatures ranging from 160 to 360 K, is shown in Fig. 4. The behavior of Z' observed in our samples shows three distinct regions in which changes are clearly visible with the change in temperature and frequency:

- At lower frequencies, in region (R-1), Z' was found to depend only on temperature; for one measuring temperature and for all compounds,

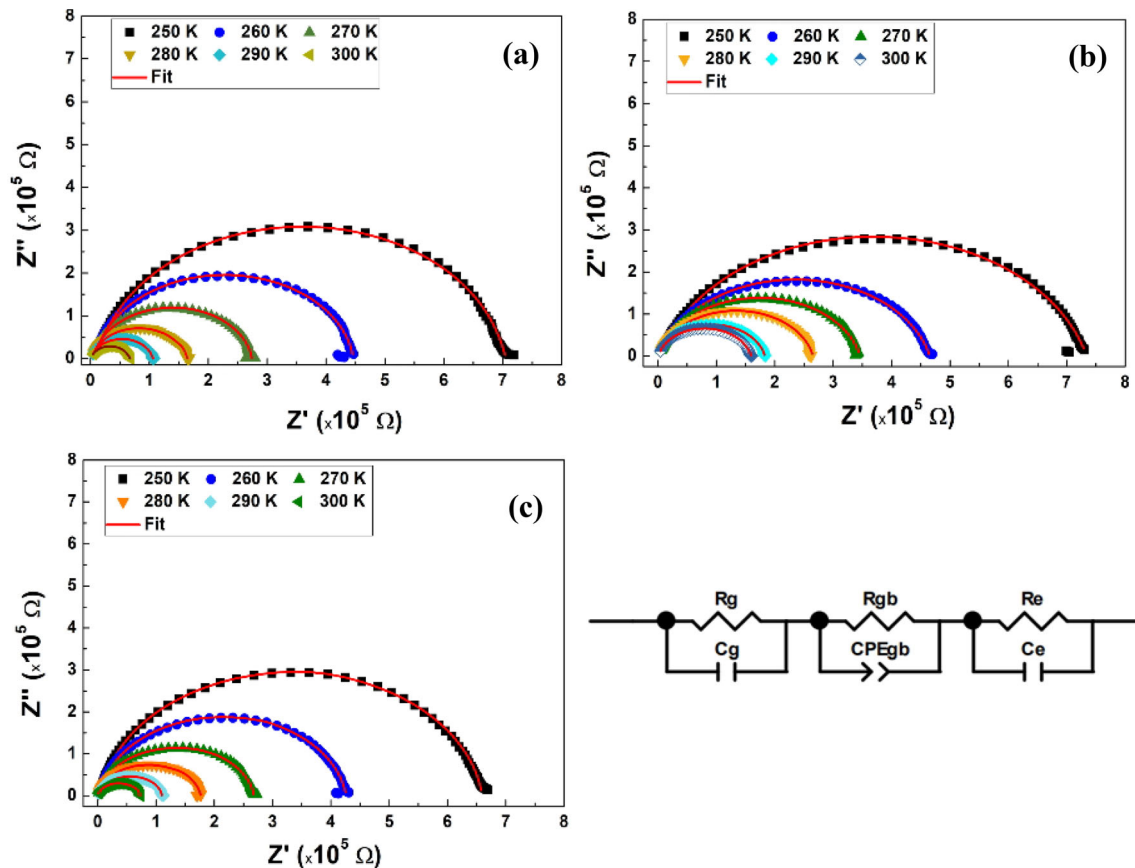


Fig. 6 Nyquist plots of impedance data at several temperatures and the equivalent circuit of $\text{La}_{0.67}\text{Ca}_{0.2}\text{Ba}_{0.13}\text{Fe}_{1-x}\text{Mn}_x\text{O}_3$ compounds: **a** $x = 0.00$, **b** $x = 0.03$, and **c** $x = 0.06$

the values of Z' are constant when rising the frequency (inset Fig. 4). This could be explained by the accumulation of charge carriers at the grain boundaries.

- In the second region (R-2), where the frequency is between about 10^4 and about 10^5 Hz (medium frequency range), the Z' values are dependent on both frequency and temperature; they decrease when frequency increases for all compounds and also they still decrease when increasing temperature. This behavior can be related to the high mobility of charge carriers. As a consequence, this causes an increase in AC conductivity with increasing temperature and frequency.
- At high frequencies (R-3), for frequencies higher than 10^5 Hz for all compounds, the real part of the complex impedance shows an independent behavior on both temperature and frequency, where all curves merge for all compounds. This behavior could possibly be related to the liberation of space charge. In fact, under the influence of

temperature, a gradual reduction of charge barrier could occur [57, 58]. Thus, improving the conduction greatly reduces resistance to AC current to become negligible.

Moreover, one can see at the medium frequency region (R-2) the presence of an inflexion that we will see is associated with a relaxation peak in the imaginary part of the complex impedance Z'' curves.

The variation of the imaginary part of the impedance (Z'') as a function of the frequency at different temperatures (160–360 K) is shown in Fig. 5. The values of (Z'') initially increase up to f_{max} then gradually decrease when the frequency and temperature increase [59]. One can see that f_{max} values are almost equal to the frequency values of inflexion points in Z' curves. Furthermore, the displacement of peaks towards high frequencies with increasing temperature indicates the presence of a relaxation phenomenon in our samples (inset of Fig. 5) [60]. The presence of these Debye-type relaxation peaks

Table 3 Values of electrical parameters deduced from the complex diagram at selected temperatures of $\text{La}_{0.67}\text{Ca}_{0.2}\text{Ba}_{0.13}\text{Fe}_{1-x}\text{Mn}_x\text{O}_3$ compounds: (a) $x = 0.00$, (b) $x = 0.03$, and (c) $x = 0.06$

(a) T(K)	Electrode contribution			Boundary grain contribution			Grain contribution		
	R($10^5 \Omega$)	CPE (10^{-11} F)	α	R($\times 10^4 \Omega$)	CPE (10^{-11} F)	α	R($10^3 \Omega$)	CPE (10^{-10} F)	α
250	9.184	3.444	0.948	4.478	4.536	0.584	6.820	1.302	0.947
260	4.338	3.727	0.947	2.237	6.877	0.736	4.298	1.998	1.048
270	2.689	3.959	0.931	1.344	8.562	1.277	3.432	2.783	1.118
280	1.488	4.335	0.922	0.874	10.122	0.459	2.428	4.300	1.911
290	0.838	4.747	0.910	0.677	21.063	0.707	1.667	3.988	0.947
300	0.498	5.020	0.898	0.376	33.23	0.479	1.185	4.563	1.111

T(K)	Electrode contribution			Boundary grain contribution			Grain contribution		
	R($10^5 \Omega$)	CPE (10^{-11} F)	α	R($\times 10^4 \Omega$)	CPE (10^{-11} F)	α	R($10^3 \Omega$)	CPE (10^{-10} F)	α
(b) 250	8.986	1.497	0.843	4.582	9.798	1.098	1.208	6.798	1.898
260	5.368	1.936	0.851	3.058	4.747	0.986	0.714	4.532	1.607
270	3.368	2.626	0.866	2.053	2.325	1.157	0.524	3.904	1.360
280	1.971	3.130	0.875	1.343	2.024	1.277	0.374	3.465	1.348
290	1.386	3.303	0.878	0.898	1.004	1.117	0.259	3.689	1.722
300	0.769	3.397	0.881	0.586	0.618	1.329	0.167	4.955	1.509
(c) 250	6.165	1.472	0.927	4.578	1.709	0.769	2.490	9.755	1.120
260	3.796	1.850	0.941	4.111	3.057	0.812	2.163	8.012	0.952
270	2.241	2.228	0.951	4.071	4.080	0.833	1.888	7.023	1.028
280	1.331	2.187	0.947	3.958	8.709	0.896	1.736	6.932	1.082
290	0.712	2.883	0.968	3.784	11.651	0.935	1.221	4.180	1.401
300	0.382	4.048	0.999	3.212	19.742	1.008	1.085	2.381	1.226

indicates the existence of spatial charges as the electrical nature of spatial charges depends on the frequency [61].

At high temperatures, there is a single relaxation peak which shifts to a higher frequency. This means that the charge carriers are thermally activated and accumulate at the grain boundaries. This also confirms the semiconductor nature of ferrites [62]. It is also noted that the peaks broaden with the increase in temperature, which indicates the appearance of a phenomenon of dielectric relaxation depending on the temperature.

Nyquist plots as a function of the frequency at different temperatures (160–360 K), of $\text{La}_{0.67}\text{Ca}_{0.2}\text{Ba}_{0.13}\text{Fe}_{1-x}\text{Mn}_x\text{O}_3$ compounds ($x = 0.00, 0.03$ and 0.06), are shown in Fig. 6. The Cole–Cole plots are characterized by the appearance of semicircles where the diameter decreases with the increasing

temperature. The diameter of the semi-circle is related to the resistance of the compound. The increase in temperature reduces the diameter of the semicircle, indicating that the conduction process is thermally activated and therefore the sample is semiconductor [63]. The presence of a single semicircular arc signifies a single relaxation phenomenon.

The Cole–Cole plots are adjusted using Z-view software [64] with combinations of equivalent circuit models presented in Fig. 6. The best fit is achieved by using an equivalent circuit, consisting of a series combination of three circuits: electrode ($R_e\text{--}C_e$), grain boundaries ($R_{gb}\text{--}CPE_{gb}$), and grain ($R_g\text{--}C_g$), where R is the resistance and CPE is the constant phase element referring to the complex element [65].

The appearance of a single semicircle is attributed to the effect of grain boundaries. It can be seen that the plots pass through the origin, which moreover

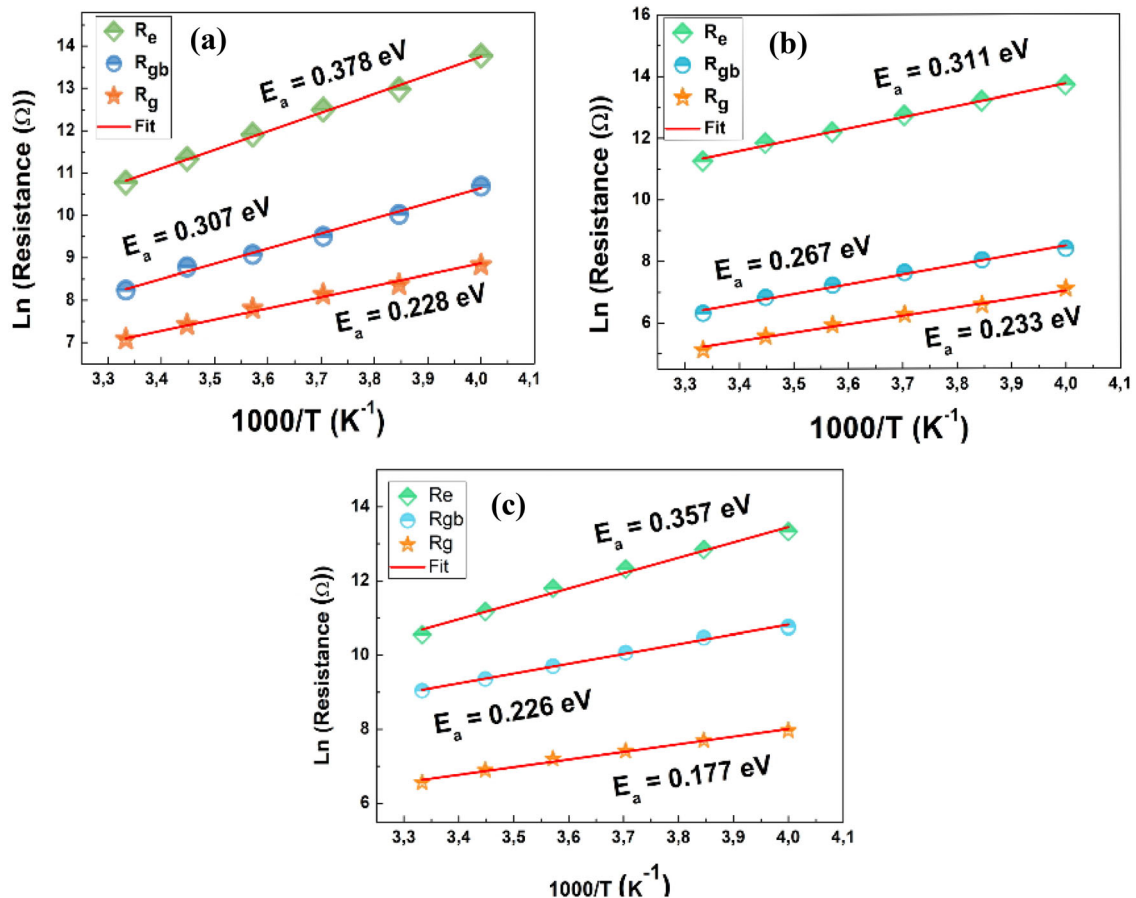


Fig. 7 The Arrhenius plots showing the dependence resistances of grain boundaries (R_{gb}) and grains (R_g) versus $1000/T$ of $\text{La}_{0.67}\text{Ca}_{0.2}\text{Ba}_{0.13}\text{Fe}_{1-x}\text{Mn}_x\text{O}_3$ compounds: **a** $x = 0.00$, **b** $x = 0.03$, and **c** $x = 0.06$

excludes the existence of a possible electrode effect. The presence of the third relaxation phenomenon (third circuit) in the Nyquist impedance plots could be attributed to the inhomogeneous distribution of oxygen. In fact, during sintering, oxygen could penetrate materials through external surfaces and move through pores and grain boundaries to occupy interstitial sites.

The values of all fitted parameters are presented in Table 3. We notice that the values of R_{gb} are larger than those of R_g , which could be due to a disorder of the atomic arrangement near the region of the grain boundaries, thus causing an increase in the diffusion of the electrons.

The activation energy can be deduced using the Arrhenius law:

$$R_{g,gb} = R_0 e^{-\frac{E_a}{k_B T}}, \quad (10)$$

where R_0 represents the pre-exponential constant or characteristic resistance, k_B is the Boltzmann constant, and E_a is the activation energy.

The logarithmic variation of R_e , R_{gb} , and R_g as a function of the inverse of the temperature is shown in Fig. 7. The value of the activation energy of the grain boundaries is greater than that of the grains, which indicates a higher resistive behavior than that of the grains.

3.5 Conductivity studies

Electrical conductivity is one of the most typical assessment tools relating the behavior of charge carriers on a macroscopic and microscopic scale. To understand electrical behavior, and determine the nature of conduction and the parameters controlling this process, we have represented in Fig. 8 the variation of the ac conductivity as a function of the

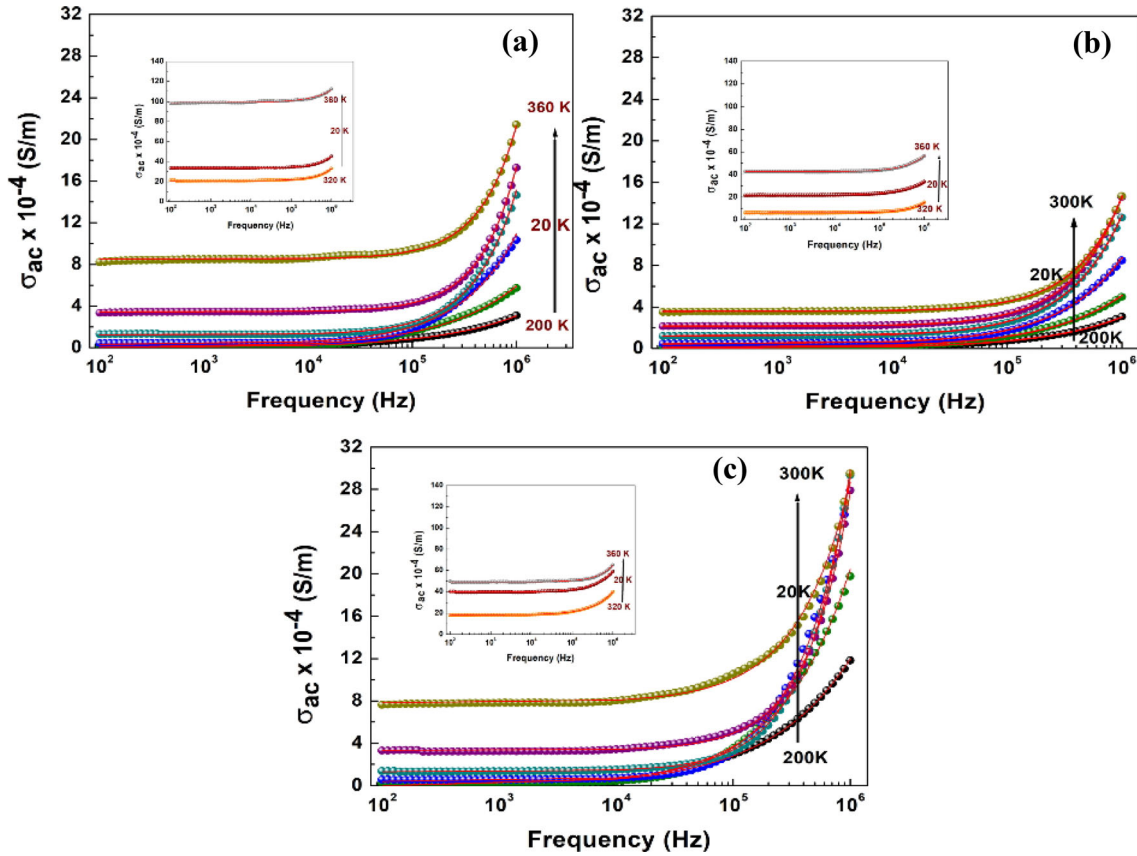


Fig. 8 Frequency dependency of conductivity for $\text{La}_{0.67}\text{Ca}_{0.2}\text{Ba}_{0.13}\text{Fe}_{1-x}\text{Mn}_x\text{O}_3$ compounds: **a** $x = 0.00$, **b** $x = 0.03$, and **c** $x = 0.06$

frequency in the temperature range 200–360 K. We noticed that there are two regions:

- At low frequencies, conductivity increases with temperature independent of frequency.
- At high frequencies, it is the dispersion region corresponding to the alternating conductivity, which increases with the increasing temperature.

The frequency dependence of the conductivity can be expressed according to Jonscher’s power law, by [66, 67]

$$\sigma(\omega) = \sigma_{dc} + \sigma_{ac} = \sigma_{dc} + A\omega^S. \tag{11}$$

In this expression, σ_{dc} and σ_{ac} describes the conductivity in continuous and alternative currents, respectively. A is a constant depending on temperature. The exponent “ S ,” which represents the degree of interaction between ions and their surroundings, represents an imperative source of information about the model for the conduction mechanism in the material.

The temperature dependence of dc conductivity at $f = 10^3$ Hz is presented in Fig. 9. In this figure we can see two different regions as a function of temperature. In the low-temperature range ($T < 250$ K), a temperature-independent behavior is detected for all compounds. In the higher region, the conductivity increases with the increase of temperature.

The logarithmic variation of dc conductivity as a function of the inverse of temperature is shown in Fig. 10. This variation can be described by the Arrhenius equation as [68]

$$\sigma_{dc} \cdot T = \sigma_0 e^{-\frac{E_a}{k_B T}}, \tag{12}$$

where σ_0 signifies the pre-exponential factor, k_B is Boltzmann constant, and E_a is the activation energy.

From the slopes of the linear fit of $\text{Ln}(\sigma_{dc} \cdot T)$ as a function of $1000/T$, we can estimate the values of the activation energies associated with dc conduction. These values are found to be 0.327, 0.275, and 0.298 eV for $x = 0, 0.03$, and 0.06 , respectively.

The ac conductivity, which obeys to the power law $A\omega^S$, increases with the increasing frequency.

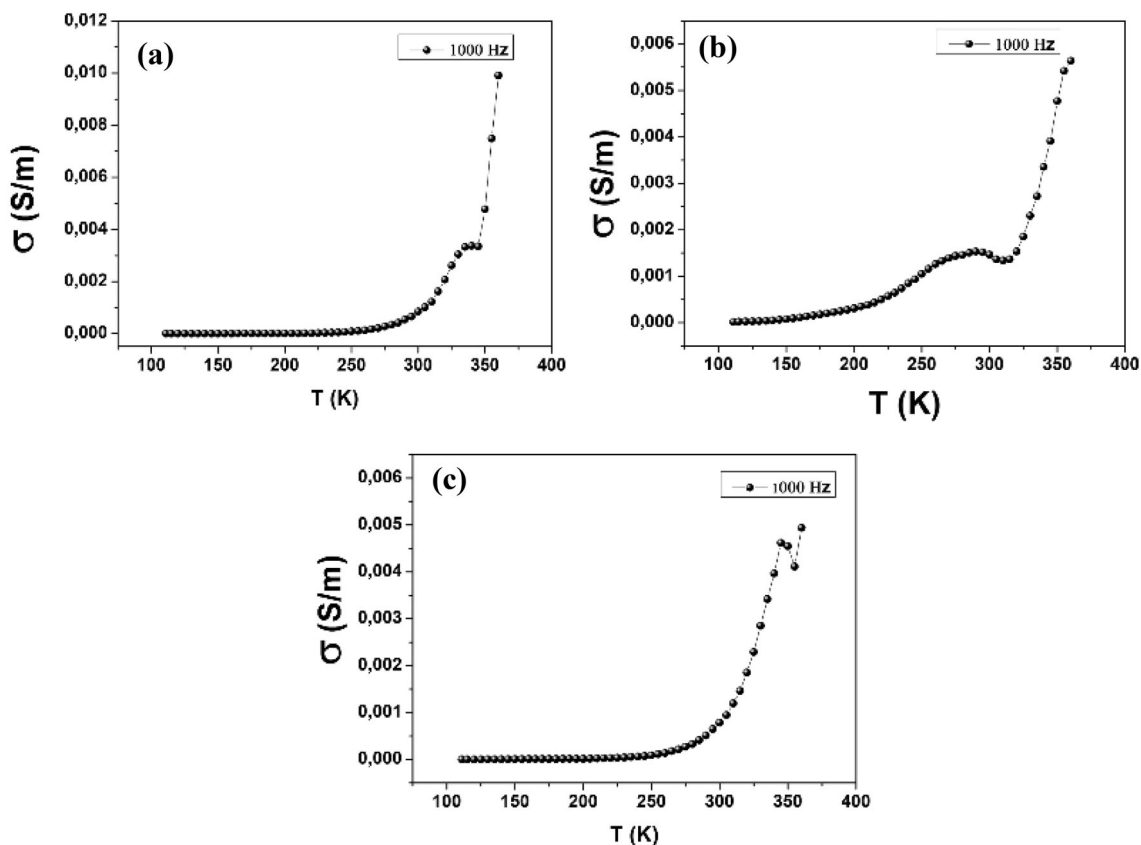


Fig. 9 Temperature dependence of dc conductivity at $f = 10^3$ Hz for **a** $x = 0.0$, **b** $x = 0.03$, and **c** $x = 0.06$

To determine the predominant conduction process for our compounds, we need to choose the appropriate model based on the Jonscher power law parameter “ S ” (Fig. 11). Based on the variation of the parameter S as a function of temperature, several models have been proposed to determine the nature of conduction, such as the Quantum Mechanical Tunneling (QMT) model where S is about 0.8 and independent of temperature [69], the Correlated Barrier Hopping (CBH) model where S decreases with the increasing temperature [70], the Non-overlapping Small Polaron Tunneling (NSPT) model where S increases with the increasing temperature [71], and the Overlapping Large Polaron Tunneling (OLPT) model where S decreases then increases with the increasing temperature [72].

- At temperatures $T < 280$ K, the exponent S increases with the increasing temperature for all three compounds, the NSPT is the appropriate model to use to describe the conduction mechanism of the three compounds in this region.

$S(T)$ can be expressed as a function of temperature by the following formula [71]:

$$S(T) = 1 + \frac{4k_B T}{W_m - k_B T \cdot \ln(\omega\tau_0)}. \quad (13)$$

W_m represents the bonding energy of charge carriers; k_B is Boltzmann’s constant; and τ_0 is the relaxation time.

For W_m very large compared to $k_B T \cdot \ln(\omega\tau_0)$, the equation of $S(T)$ becomes

$$S(T) = 1 + \frac{4k_B T}{W_m}. \quad (14)$$

The values of W_m were deduced from the slope of the $S(T)$ curves in the CBH behavior. The values are obtained in the order of 0.038 eV, 0.043, and 0.086 eV for $x = 0, 0.03$, and 0.06 , respectively. The insertion of manganese in place of iron has an effect on the bonding energy.

- At $T > 280$ K,

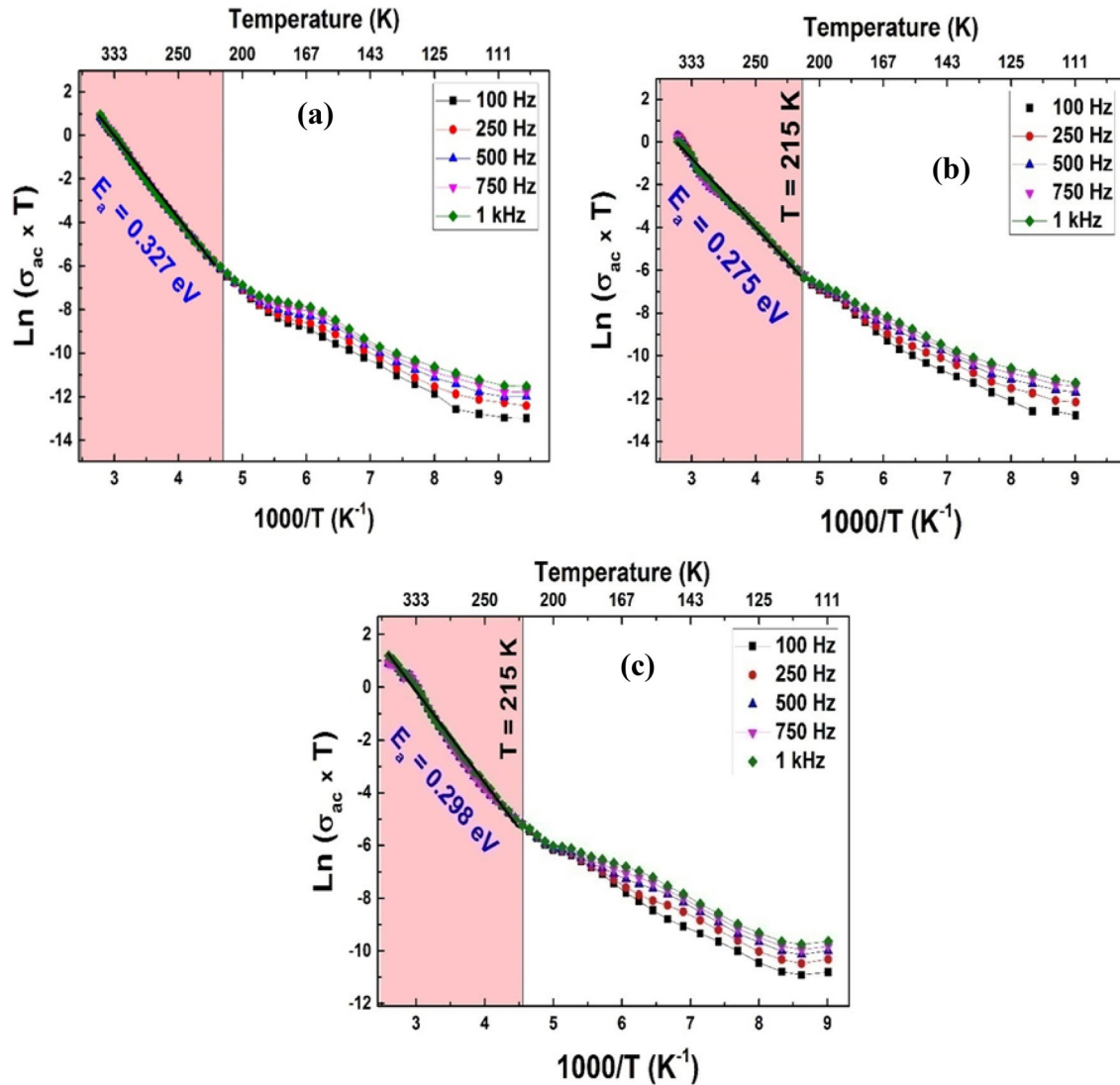


Fig. 10 Variation of the $\text{Ln}\sigma_{\text{dc}}$ as a function $1000/T$ of $\text{La}_{0.67}\text{Ca}_{0.2}\text{Ba}_{0.13}\text{Fe}_{1-x}\text{Mn}_x\text{O}_3$ compounds **a** $x = 0.00$, **b** $x = 0.03$, and **c** $x = 0.06$

- For $x = 0$, the evolution of S as a function of temperature indicates that the CBH is the very excellent theoretical model for describing the mechanism of electrical conduction. This model depicts the jumps of charge carriers between sites above the potential barrier separating them.

In this model, $S(T)$ is given by

$$S(T) = 1 - \frac{6k_B T}{W_m - k_B T \cdot (1 - \omega\tau_0)}. \tag{15}$$

For the large values of $\frac{W_m}{k_B T}$, the above equation (Eq. 15) was approximated and became [73]

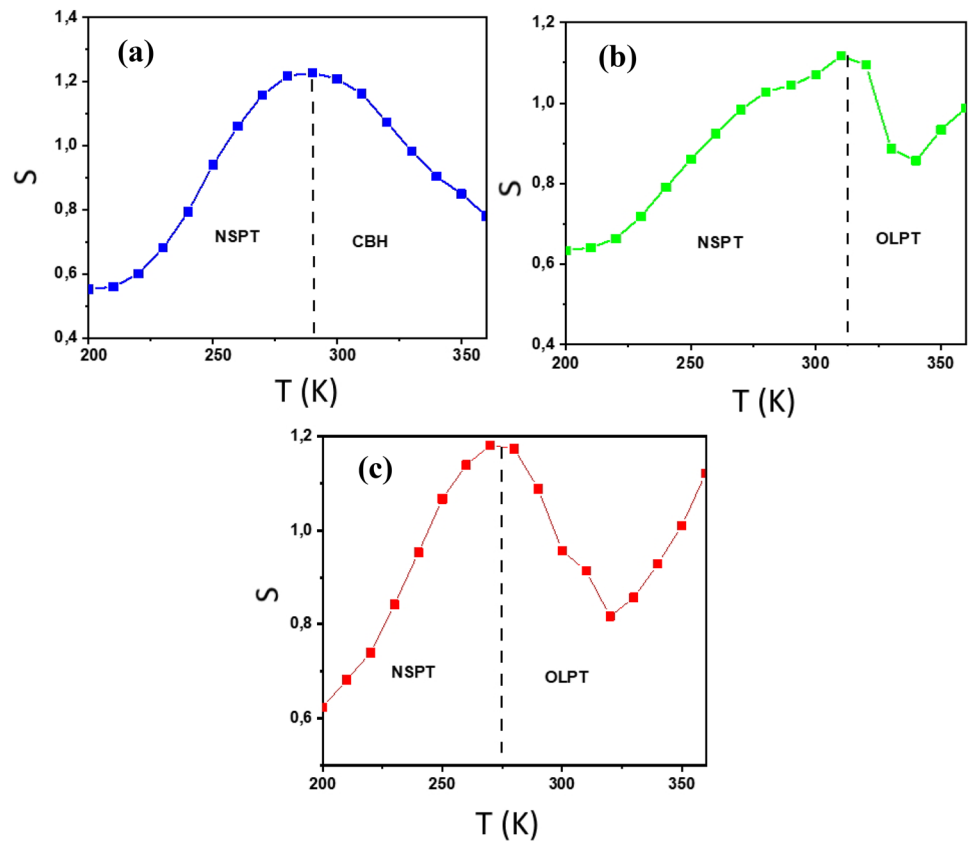
$$S(T) = 1 - \frac{6k_B T}{W_m}. \tag{16}$$

The energy W_m , required to move an electron from one site to another, was deduced from the slope of $(1 - S)$ as a function of temperature. It is equal to 0.086 eV. We notice the increase in the W_m value with the increase in temperature, which corresponds to the decrease in the exponent S . Thus, the number of free carriers who can jump over the barrier will increase [74].

- For $x = 0.03$ and 0.06 .

The variation of the “ S ” parameter as a function of temperature suggests that the OLPT model is the most suitable model to characterize the electrical

Fig. 11 Temperature dependence of the exponent S of $\text{La}_{0.67}\text{Ca}_{0.2}\text{Ba}_{0.13}\text{Fe}_{1-x}\text{Mn}_x\text{O}_3$ compounds **a** $x = 0.00$, **b** $x = 0.03$, and **c** $x = 0.06$



conduction mechanism in the $x = 0.03$ and $x = 0.06$ compounds, respectively. We can conclude that the substitution of Fe by Mn largely influences the conduction mechanism.

One of the fundamental characteristics of ferrites is the strong correlation between microstructure and physical properties. Our compounds have high electrical properties and good thermal and chemical stability. They are susceptible to many technological applications, such as capacitors, gas sensor, new read heads, and solid oxide fuel cells.

4 Conclusion

We have synthesized $\text{La}_{0.67}\text{Ca}_{0.2}\text{Ba}_{0.13}\text{Fe}_{1-x}\text{Mn}_x\text{O}_3$ compounds ($x = 0.00, 0.03$, and 0.06) by the auto-combustion method. Our results show that the XRD patterns of the synthesized samples present a single phase. The crystallite size value measured using Scherrer's formula was found in the range of 28 to 17 nm. The nanosize criteria were also confirmed by the Williamson–Hall method. Analysis of impedance plots in the frequency range 100 to 10^6 Hz and in the

temperature range 160 to 360 K showed a decrease in electrical resistance. The contribution of grain boundaries is greater than that of grains. The charge carriers are thermally activated and accumulate at the grain boundaries, confirming the semiconductor nature of materials. The impedance spectra are characterized by the appearance of semicircular arcs, well modeled in terms of electrical equivalent circuit confirming the contribution of the grain and grain boundaries. The Jonscher's power law is well fitted to the ac conductivity data. This ac conductivity analysis shows that the substitution of Fe by Mn affects the conduction mechanism model. The suitable model for all three samples is the NSPT for $T < 280$ K, while it is the CBH model for $x = 0$ and OLPT model for both samples $x = 0.03$ and $x = 0.06$ above 280 K.

The insertion of Mn in small quantities has a significant impact on the electrical properties of the compounds. This study was useful to understand the effect of Mn substitution on electrical and dielectric properties and present information for the use of these nanomaterials in high frequency devices, capacitors, and gas sensor.

Acknowledgements

CFisUC is supported by national funds from FCT – Fundação para a Ciência e a Tecnologia, I.P., within the projects UIDB/04564/2020 and UIDP/04564/2020. Access to TAIL-UC facility funded under QREN-Mais Centro Project No. ICT_2009_02_012_1890 is gratefully acknowledged.

Compliance with ethical standards

Conflict of interest There are no conflicts of interest to declare.

References

- M.C. Carotta, M.A. Butturi, G. Martinelli, Y. Sadaoka, P. Nunziante, E. Traversa, *Sens. Actuators B* **44**, 590 (1997)
- E.A. Tugova, V.F. Popova, I.A. Zvereva, V.V. Gusarov, *Phys. Chem.* **32**, 674 (2006)
- D. Makovec, A. Kodre, I. Arčon, M. Drogenik, *J. Nanopart. Res.* **11**(5), 1145 (2009)
- S.G. Krishnan, M.V. Reddy, M. Harilal, B. Vidyadharan, I.I. Misnon, M.H. Ab Rahim, J. Ismail, R. Jose, *Electrochim. Acta* **161**, 312 (2015)
- F. Wang, Y. Liu, Y. Zhao, Y. Wang, Z. Wang, W. Zhang, F. Ren, *Appl. Sci.* **8**(1), 22 (2018)
- S. Sahoo, K.K. Naik, C.S. Rout, *Nanotechnology* **26**(45), 455401 (2015)
- H. Gao, S. Liu, Y. Li, E. Conte, Y. Cao, *Energies* **10**(11), 1787 (2017)
- S.N. Tijare, M.V. Joshi, P.S. Padole, P.A. Mangrulkar, S.S. Rayalu, N.K. Labhsetwar, *Int. J. Hydrog. Energy* **37**, 10451 (2012)
- M. Viret, D. Rubi, D. Colson, D. Lebeugle, A. Forget, P. Bonville, G. Dhalenne, R. Saint-Martin, G. Andre, F. Ott, *Mater. Res. Bull.* **47**, 2294 (2012)
- H. Xiao, C. Xue, P. Song, J. Li, Q. Wang, *Appl. Surf. Sci.* **337**, 65 (2015)
- S.J. Xu, W.J. Thomson, *AIChE J.* **43**, 2731 (1997)
- C.Y. Tsai, A.G. Dixon, W.R. Moser, Y.H. Ma, *AIChE J.* **43**, 2741 (1997)
- E.V. Tsipis, M.V. Patrakeev, V.V. Kharton, A.A. Yaremchenko, G.C. Mather, A.L. Shaula, I.A. Leonidov, V.L. Kozhevnikov, J.R. Frade, *Solid State Sci.* **7**, 355 (2005)
- I. Hole, T. Tybell, J.K. Grepstad, I. Waernhus, T. Grande, K. Wiik, *Solid State Electron* **47**, 2279 (2003)
- Y.R. Pei, Y. Li, J.Y. Che, W.Z. Shen, Y.C. Wang, S.Q. Yang, S.M. Han, *Int. J. Hydrog. Energy* **40**(28), 8742 (2015)
- K. Huang, H.Y. Lee, J.B. Goodenough, *J. Electrochem. Soc.* **145**, 3220 (1999)
- R. Chiba, F. Yoshimura, Y. Sakurai, *Solid State Ionics* **152–153**, 575–582 (2002)
- A.A. Yaremchenko, M.V. Patrakeev, V.V. Kharton, F.M.B. Marques, I.A. Leonidov, V.L. Kozhevnikov, *Solid State Sci.* **6**, 357–366 (2004)
- G. Coffey, J. Hardy, O. Marina, L. Pederson, P. Rieke, E. Thomsen, *Solid State Ionics* **175**, 73 (2004)
- G. Zhu, X. Fang, C. Xia, X. Liu, *Ceram. Int.* **31**, 115 (2005)
- W.G. Wang, M. Mogensen, *Solid State Ionics* **176**, 457 (2005)
- A. Mai, V.A.C. Haanappel, S. Uhlenbruck, F. Tietz, D. Stover, *Solid State Ionics* **176**, 1341 (2005)
- Z.X. Wei, Y.Q. Xu, H.Y. Liu, C.W. Hu, *J. Hazard. Mater.* **165**, 1056 (2009)
- P. Xiao, L. Zhong, J. Zhu, J. Hong, J. Li, H. Li, Y. Zhu, *Catal. Today* **258**, 660 (2015)
- E.M. Benali, A. Benali, M. Bejar, E. Dhari, M.P.F. Graça, M.A. Valente, P. Sanguino, B.F.O. Costa, *J. Mater. Sci., Mater. Electr.* **31**, 16220–16234 (2020)
- E. Cao, Y. Qin, T. Cui, L. Sun, W. Hao, Y. Zhang, *Ceram. Int.* **43**, 7922 (2017)
- S. Phokha, S. Hunpratup, S. Pinitsoontorn, B. Pustasaeng, S. Rujirawat, S. Maensiri, *Mater. Res. Bull.* **67**, 118 (2015)
- L. Sun, H. Qin, K. Wang, M. Zhao, J. Hu, *Mater. Chem. Phys.* **125**, 305–308 (2011)
- G. Md, B.K. Masud, H.D. Yang, *J. Phys. D* **44**, 255403 (2011)
- X.P. Xiang, L.H. Zhao, B.T. Teng, J.J. Lang, X. Hu, T. Li, Y.A. Fang, M.F. Luo, J.J. Lin, *Appl. Surf. Sci.* **276**, 328 (2013)
- F.B. Abdallah, A. Benali, S. Azizi, M. Triki, E. Dhahri, M.P.F. Graça, M.A. Valente, *J. Mater. Sci.* **30**, 8457 (2019)
- F.B. Abdallah, A. Benali, M. Triki, E. Dhahri, K. Nomenyo, G. Lerondel, *J. Mater. Sci.* **30**, 3349 (2019)
- A. Benali, S. Azizi, M. Bejar, E. Dhahri, M.F.P. Graça, *Ceram. Int.* **40**, 14367 (2014)
- A. Benali, A. Souissi, M. Bejar, E. Dhahri, M.F.P. Graça, M.A. Valente, *Chem. Phys. Lett.* **637**, 7 (2015)
- H. Han, J.S. Lee, J.H. Ryu, K.M. Kim, J.L. Jones, J. Lim, S. Guillemet-Fritsch, H.C. Lee, S. Mhin, *J. Phys. Chem. C* **120**(25), 13667–13674 (2016)
- R.A. Young, *The Rietveld Method* (Oxford University Press, New York, 1993).
- T. Roisnel, J. Rodriguez-Carvajal, *Computer Program FULL-PROF, LLB-LCSIM*, 2003.
- M.M.K. Costa, G.F.M. Pires Junior, A.S.B. Sombra, *Mater. Chem. Phys.* **123**, 35 (2010)
- R.D. Shannon, *Acta Crystallogr.* **32**, 751 (1976)
- J. Kanamori, *J. Appl. Phys. Suppl.* **31**, 145 (1960)

41. S.K. Abdel-Aal, A.S. Abdel-Rahman, *J Nanopart Res.* **22**, 267 (2020). <https://doi.org/10.1007/s11051-020-05001-7>
42. D.R. Lide, *CRC Handbook of Chemistry and Physics: A Ready-Reference Book of Chemical and Physical Data* (CRC Press, Boca Raton, 1995).
43. M.A. Khan, M. Islam, M. Ishaque, I. Rahman, A. Genson, S. Hampshire, *Mater. Character.* **60**(1), 73 (2009)
44. S. Nasrin, S.M. Hoque, F.-U.-Z. Chowdhury, M.M. Hossen, *J. Appl. Phys.* **6**, 58 (2014)
45. A.V. Humbe, A.C. Nawle, A.B. Shinde, K.M. Jadhav, *J. Alloy. Compd.* **691**, 343 (2017)
46. S.G. Kakade, R.C. Kambale, C.V. Ramanna, Y.D. Kolekar, *RSC Adv.* **6**, 33308 (2016)
47. M. Georgea, A.M. Johna, S.S. Naira, P.A. Joy, M.R. Anantharaman, *J. Magn. Magn. Mater.* **302**, 190 (2006)
48. L. Aswaghosh, D. Manoharan, N.V. Jaya, *Phys. Chem. Chem. Phys.* **18**, 5995 (2016)
49. E.R. Kumar, C. Sirinivas, M.S. Seehra, M. Deepty, I. Pradeep, A.S. Kamzin, M.V.K. Mehar, N.K. Mohan, *Sens. Actuators A* **279**, 10–16 (2018)
50. V.M. Goldschmidt, *Geochemistry* (Oxford University Press, Oxford, 1958).
51. S. Manzoor, S. Husain, A. Somvanshi, M. Fatema, *J. Mater. Sci.* **31**, 7811 (2020)
52. A. Somvanshi, S. Husain, W. Khan, *J. Alloy. Compd.* **778**, 439 (2019)
53. A. Somvanshi, S. Husain, S. Manzoor, N. Zarrin, W. Khan, *J. Alloy Compd.* **806**, 1250 (2019)
54. S. Manzoor, S. Hussain, *J. Appl. Phys.* **124**, 065110 (2018)
55. A.K. Baral, V. Sankaranarayanan, *Appl. Phys. A* **98**, 367 (2010)
56. V. Saltas, I. Fitis, F. Vallianatos, *Tectonophysics* **637**, 198 (2014)
57. S. Brahma, R.N.P. Choudhary, A.K. Thakur, *Phys. B* **355**, 188 (2005)
58. F.B. Abdallah, A. Benali, M. Triki, E. Dhahri, M.P.F. Graca, M.A. Valente, *Superlatt. Microstruct.* **117**, 260 (2018)
59. H. Baaziz, N.K. Maaloul, A. Tozri, H. Rahmouni, S. Mizouri, K. Khirouni, E. Dhahri, *Chem. Phys. Lett.* **640**, 77 (2015)
60. A. Omri, M. Bejar, E. Dhahri, M. Es-Souni, M.A. Valente, M.P.F. Graca, L.C. Costa, *J. Alloys Compd.* **536**, 173 (2012)
61. D.L. Sekulic, Z.Z. Lazarevic, C.D. Jovalekic, A.N. Milutinovic, N.Z. Romcevic, *SciSinte* **48**(1), 17 (2016)
62. M.E. Hajlaoui, R. Dhahri, N. Hnainia, A. Benchaabane, E. Dhahri, K. Khirouni, *RSC Adv.* **9**, 32395 (2019)
63. M. Satalkar, S.N. Kane, M. Kumaresavanji, J.P. Araujo, *Mater. Res.* **91**, 14 (2017)
64. D. Johnson, *Z Plot, Z View Electrochemical Impedance Software, Version 2.3b* (Scribner Associates, Inc., North Carolina, 2000).
65. D. Suresh, R. Udayabhanu, M.A. PavanKumar, H. Nagabhushana, S.C. Sharma, *Mater. Lett.* **151**, 93 (2015)
66. A.K. Jonscher, *Nature* **267**(5613), 673 (1977)
67. A.K. Jonscher, *J. Phys. D* **32**, R57 (1999)
68. K.P. Padmasree, D.K. Kanchan, A.R. Kulkarni, *Solid State Ionics* **177**, 475 (2006)
69. M. Pollak, *Philos. Magn.* **23**, 519 (1971)
70. S. Mollah, K.K. Som, K. Bose, B.K. Chaudhuri, *J. Appl. Phys.* **74**, 931 (1993)
71. A. Ghosh, *Phys. Rev. B* **41**, 1479 (1990)
72. M. Megdiche, C. Perrin-Pellegrino, M. Gargouri, *J. Alloys Compd.* **584**, 209 (2014)
73. K.H. Mahmoud, F.M. Abdel-Rahim, K. Atef, Y.B. Saddeek, *Curr. Appl. Phys.* **11**, 55 (2011)
74. Y.B. Taher, A. Oueslati, N.K. Maaloul, K. Khirouni, M. Gargouri, *Appl. Phys. A* **120**, 1537 (2015)

Publisher's Note Springer Nature remains neutral with regard to jurisdictional claims in published maps and institutional affiliations.

Terms and Conditions

Springer Nature journal content, brought to you courtesy of Springer Nature Customer Service Center GmbH (“Springer Nature”).

Springer Nature supports a reasonable amount of sharing of research papers by authors, subscribers and authorised users (“Users”), for small-scale personal, non-commercial use provided that all copyright, trade and service marks and other proprietary notices are maintained. By accessing, sharing, receiving or otherwise using the Springer Nature journal content you agree to these terms of use (“Terms”). For these purposes, Springer Nature considers academic use (by researchers and students) to be non-commercial.

These Terms are supplementary and will apply in addition to any applicable website terms and conditions, a relevant site licence or a personal subscription. These Terms will prevail over any conflict or ambiguity with regards to the relevant terms, a site licence or a personal subscription (to the extent of the conflict or ambiguity only). For Creative Commons-licensed articles, the terms of the Creative Commons license used will apply.

We collect and use personal data to provide access to the Springer Nature journal content. We may also use these personal data internally within ResearchGate and Springer Nature and as agreed share it, in an anonymised way, for purposes of tracking, analysis and reporting. We will not otherwise disclose your personal data outside the ResearchGate or the Springer Nature group of companies unless we have your permission as detailed in the Privacy Policy.

While Users may use the Springer Nature journal content for small scale, personal non-commercial use, it is important to note that Users may not:

1. use such content for the purpose of providing other users with access on a regular or large scale basis or as a means to circumvent access control;
2. use such content where to do so would be considered a criminal or statutory offence in any jurisdiction, or gives rise to civil liability, or is otherwise unlawful;
3. falsely or misleadingly imply or suggest endorsement, approval, sponsorship, or association unless explicitly agreed to by Springer Nature in writing;
4. use bots or other automated methods to access the content or redirect messages
5. override any security feature or exclusionary protocol; or
6. share the content in order to create substitute for Springer Nature products or services or a systematic database of Springer Nature journal content.

In line with the restriction against commercial use, Springer Nature does not permit the creation of a product or service that creates revenue, royalties, rent or income from our content or its inclusion as part of a paid for service or for other commercial gain. Springer Nature journal content cannot be used for inter-library loans and librarians may not upload Springer Nature journal content on a large scale into their, or any other, institutional repository.

These terms of use are reviewed regularly and may be amended at any time. Springer Nature is not obligated to publish any information or content on this website and may remove it or features or functionality at our sole discretion, at any time with or without notice. Springer Nature may revoke this licence to you at any time and remove access to any copies of the Springer Nature journal content which have been saved.

To the fullest extent permitted by law, Springer Nature makes no warranties, representations or guarantees to Users, either express or implied with respect to the Springer nature journal content and all parties disclaim and waive any implied warranties or warranties imposed by law, including merchantability or fitness for any particular purpose.

Please note that these rights do not automatically extend to content, data or other material published by Springer Nature that may be licensed from third parties.

If you would like to use or distribute our Springer Nature journal content to a wider audience or on a regular basis or in any other manner not expressly permitted by these Terms, please contact Springer Nature at

onlineservice@springernature.com